

Entering Voltage Hysteresis in Phase-Separating Materials: Revealing the Electrochemical Signature of the Intraparticle Phase-Separated State

Tomaž Katrašnik,* Jože Moškon, Klemen Zelič, Igor Mele, Francisco Ruiz-Zepeda, and Miran Gaberšček*

Hysteresis is a general phenomenon regularly observed in various materials. Usually, hysteretic behavior is an intrinsic property that cannot be circumvented in the nonequilibrium operation of the system. Herein, it is shown that, at least with regard to the hysteretic behavior of phase-separating battery materials, it is possible to enter (deeply) the hysteretic loop at finite battery currents. This newly observed electric response of the electrode, which is inherent to phase-separating materials, is related to its microscopic origin arising from a (significant) share of the active material residing in an intraparticle phase-separated state. This intriguing observation is further generalized by revealing that a phase-separating material can feature (significantly) different chemical potentials at the same bulk lithiation level and temperature when exposed to the same finite current and external voltage hysteresis. Therefore, the intraparticle phase-separated state significantly affects the DC and AC characteristics of the battery. The experimental evidence for entering the intraparticle phase-separated state is supported by thermodynamic reasoning and advanced modeling. The current findings will help advance the understanding, control, diagnostics, and monitoring of batteries composed of phase-separating materials while also providing pertinent motivation for the enhancement of battery design and performance.

1. Introduction

Lithium iron phosphate (LFP)-based batteries, as well as their mixed analogs, such as lithium iron manganese phosphate batteries, are gaining importance owing to their high safety, high power density, acceptable energy density, durability, lack of resource-limiting critical metals, and especially their excellent price-performance ratio.^[1,2] This opens the way for them to enter the mass market of electromobility and large-scale energy storage, as well as other application areas. Short- and medium-term energy storage and transport applications are characterized by highly dynamic operating regimes; however, these applications require the precise monitoring and control of a large number of cells to ensure their proper operation, longevity, and safety.^[3–6] Batteries containing other phase-separating materials, such as lithium titanate oxide (LTO)^[7,8] and lithium manganese phosphate (LMP), have also been widely used.

Despite significant progress in understanding the phenomena in phase-separating materials,^[7,9–11] the phase-separation reactions in real electrodes remain poorly understood. This is largely because of the high complexity of battery electrodes, which consist of numerous particles interconnected by binders and conductive additives.^[7,12] There are still many electrochemical phenomena that cannot be clearly and unambiguously explained by underlying changes in the composition, structure, and microstructure of the materials that constitute a battery electrode.

An example of a seminal work establishing a quantitative relationship between the general electrochemical performance and the corresponding phase transformation in phase-separating battery materials is the work by Dreyer et al.^[10] published more than a decade ago. The authors developed a thermodynamic model that explained the widely observed inherent (zero-current) voltage hysteresis in phase-transforming materials by accounting for the microscopic and structural changes observed in electrodes composed of phase-separating particles. These findings have been elaborated in several follow-up studies.^[13–16] Other well-known phenomena relating to the macroscopic electrochemical

T. Katrašnik, K. Zelič, I. Mele
Faculty of Mechanical Engineering
University of Ljubljana
Aškerčeva 6, Ljubljana SI-1000, Slovenia
E-mail: tomaz.katrasnik@fs.uni-lj.si

J. Moškon, F. Ruiz-Zepeda, M. Gaberšček
Department of Materials Chemistry
National Institute of Chemistry
Hajdrihova 19, Ljubljana SI-1000, Slovenia
E-mail: miran.gaberscek@ki.si

M. Gaberšček
Faculty of Chemistry and Chemical Technology
University of Ljubljana
Večna pot 113, Ljubljana SI-1000, Slovenia

 The ORCID identification number(s) for the author(s) of this article can be found under <https://doi.org/10.1002/adma.202210937>

© 2023 The Authors. Advanced Materials published by Wiley-VCH GmbH. This is an open access article under the terms of the Creative Commons Attribution License, which permits use, distribution and reproduction in any medium, provided the original work is properly cited.

DOI: 10.1002/adma.202210937

output and underlying microscopic processes in active materials include the so-called “memory effect”^[16] and “group-by-group” multiparticle Li intercalation in a battery system undergoing Li phase separation leading to electrochemical oscillations.^[7] Although various mechanisms have been identified, the model developed by Dreyer et al.,^[10] which tacitly assumes that hysteresis cannot be avoided in phase-separating materials, remains unchallenged. However, in this study, we challenge this basic assumption by attempting to answer the following fundamental dilemma: Is it possible to enter the hysteresis loop under dynamic operating conditions?

In the context of this study, it is important to distinguish between the hysteretic effects^[17] of thermodynamic origin and different types of overpotentials. Overpotentials have a kinetic origin and can be minimized, for example, by systematically reducing the charge or discharge rate,^[17] and eventually eliminated in the asymptotic limit of exceedingly slow charge and discharge currents. This does not apply to hysteretic effects of thermodynamic origin, which cannot be avoided, except in very rare cases.^[18–21] Several battery papers have clearly shown that the hysteretic behavior of phase-transitioning battery materials is ubiquitous.^[22–29] Only occasionally do published measurements indicate voltages that are apparent within the hysteretic loop.^[10,30] Recently, entry into a hysteretic loop has been reported for Si electrodes.^[31,32] However, it must be emphasized that lithiated silicon is not a typical phase-separating material^[32,33]; therefore, the thermodynamic background, which is still not entirely clear, may be different from the present case.

As for phase-separating materials, many studies have confirmed the existence of inherent voltage hysteresis.^[13,15,25,34–41] Considering the ubiquity of this phenomenon, it seems more or less impossible for the active material to exist in a state that increases its potential to a level that allows entry into the inherent hysteretic loop (close to the equilibrium state) of a battery at finite currents. Similarly, based on current knowledge, it seems impossible for a phase-separating material to form an electrode that has (significantly) different chemical potentials when exposed to the same finite current at the same lithium content and temperature.

In this study, we challenge the existing views on hysteretic properties, both theoretically and experimentally. We identified and discussed new correlations among several material-related phenomena. First, we demonstrate an innovative pulse-based electrochemical experiment that generates numerous long-lived intraparticle phase-separated states, in which the adjacent phases are either Li-rich or Li-poor. The existence of these electrochemically induced intraparticle separated states was proven using *ex situ* scanning transmission electron microscopy–electron energy-loss spectroscopy (STEM-EELS). Thus, we demonstrated the existence of a new material state characterized by its own chemical potential, which is significantly different from the chemical potentials of other known phase-forming battery materials.^[10,15,40,42] It is further shown that using various dynamic excitation protocols, it is possible to switch from the interparticle to the intraparticle phase-separated state of the active material, i.e., that it is possible to manipulate the material to adopt different values of chemical potential depending on its history. This possibility has major implications for future battery applications, where the determination of accurate potential values and

their control are crucial, as briefly discussed in the last part of the paper.

2. Results and Discussion

2.1. Key Experimental Evidence

The basic electrochemical performance of the battery-grade “Targray LFP” cathode material is shown in Figure S1A, Supporting Information, which indicates that it exhibits good electrochemical performance with excellent capacity retention at high current densities. Moreover, the results of the classical galvanostatic intermittent titration technique (GITT, Figure S1B, Supporting Information) show a well-developed voltage plateau because of the equilibrium between the coexisting Li-poor ($\text{Li}_\alpha\text{FePO}_4$) and Li-rich ($\text{Li}_\beta\text{FePO}_4$) phases with a corresponding equilibrium voltage of 3.428 V vs metal-lithium (Li^+/Li^0).

A direct bridge between the macroscopic electrochemical output of a phase-separating battery material and the corresponding microscopic processes occurring in the individual active particles of an LFP material is shown in Figure 1a–c, respectively. Here “particle” denotes either a single primary storage particle or an aggregate.^[43] The blue curve in Figure 1a corresponds to a regular charge-discharge cycle at a low (dis)charge rate (C/100), whereas the red dashed curve shows the potential evolution upon application of the so-called dynamic excitation (the initial $-C/100$ rate is switched to $-5C$ and then returned to $-C/100$), as indicated in the legend. It is clear that after the latter switch (from high to low C-rates), the red curve enters deeply into the blue-shaded hysteretic area, which until now seemed unattainable at finite battery currents.

At first glance, the results shown in Figure 1a seem to contradict the original particle-by-particle lithiation process at low currents, which explains the existence of hysteresis postulated by Dreyer et al.^[10] However, as shown in the continuation, the reason for the observed behavior is not a flaw or deficiency of the model by Dreyer et al.,^[10] but a result of the simultaneous entrance of a large share of the active particle population into the intraparticle phase-separated state.

To determine the underlying reason(s) for the unusual electrochemical behavior shown in Figure 1a, we systematically analyzed the material changes occurring during high-current stimuli. Because the storage mechanism in the present material involves compositional changes, that is, a reversible $\text{Fe}^{2+}/\text{Fe}^{3+}$ redox reaction occurring within individual LFP particles, we performed STEM-EELS. It is to be noted that both the electrochemical as well as STEM-EELS experiments were purposefully performed on a commercial battery-grade (“Targray”) LFP material with good electrochemical performance. Specifically, we wanted to focus on general phenomena, that is, phenomena that also occur and are relevant in realistic materials, rather than on phenomena found mainly in special materials with laboratory-tailored sizes and structural, compositional, and other features. However, to perform reliable and correct STEM-EELS analysis on realistic battery materials involving various inhomogeneities, a special centrifugation separation procedure step was applied before electrode preparation. This way, we selectively removed the largest LFP aggregates from the starting Targray LFP powder (see Experimental procedures). Only the fraction that included thin

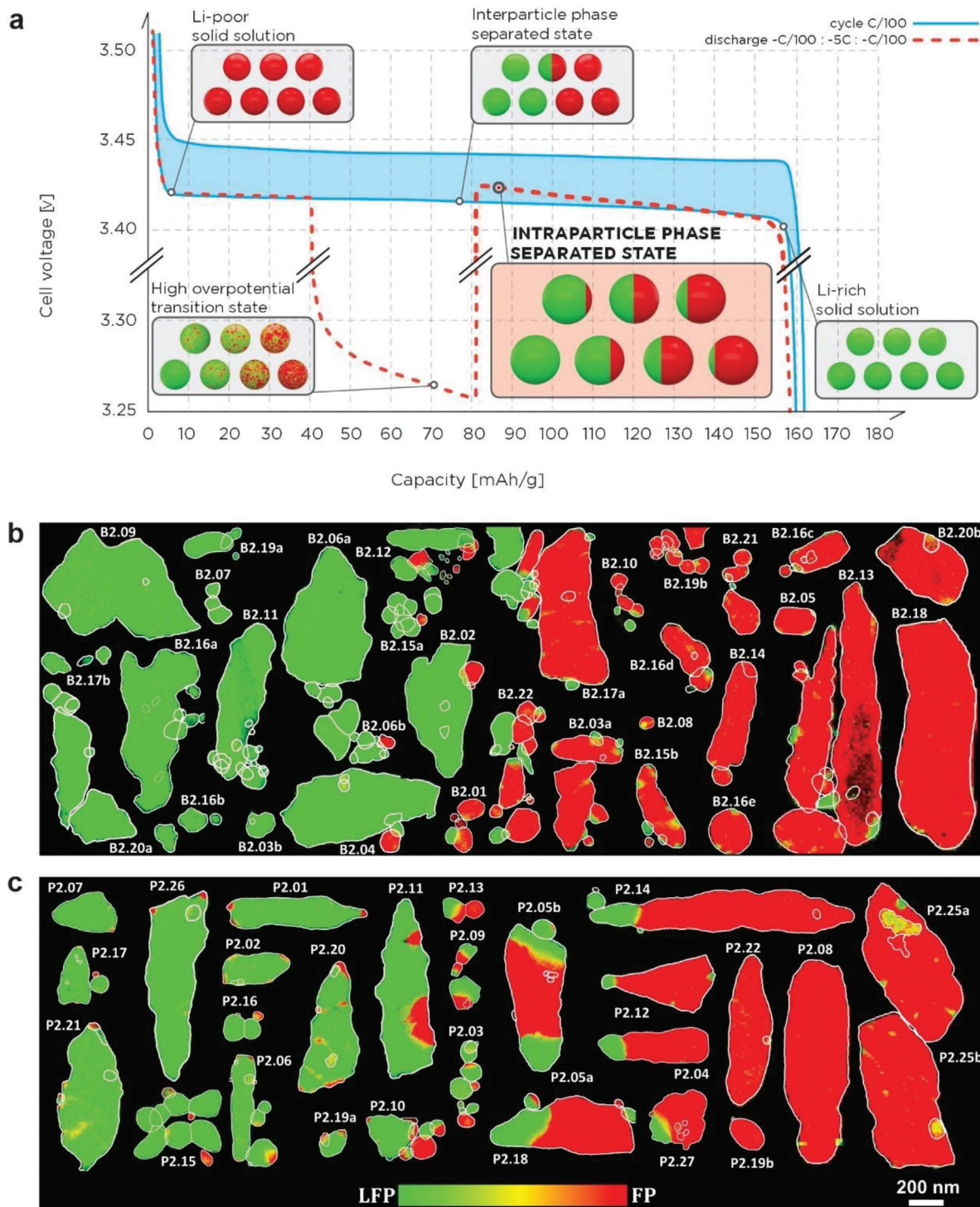


Figure 1. a) Path-dependent entrance into the voltage hysteresis in phase-separating battery materials. The blue curve shows the conventionally observed voltage hysteresis of LFP at small currents (measured on cell #1). The red curve demonstrates the entrance into the hysteretic loop after reducing the current from the preceding current stimulus (starting at 25% and ending at 50% depth-of-discharge (DOD)) applied during a battery discharge. The entrance into the voltage hysteretic loop is explained by an intraparticle phase-separated state depicted by the central scheme. This state is fundamentally different compared to the other frequently encountered electrode states, which comprise solid solution state at low and high lithiation levels,^[15,40,42] high-overpotential transient state within the miscibility gap^[15,40,42] (more details provided in Section S3.2, Supporting Information) under the application of a large current, and interparticle phase-separated state^[11] or mosaic instability^[14] being characterized by a particle-by-particle mode of lithiation^[10] under application of a small current without preceding current stimulus. b,c) STEM-EELS color map demonstrating the interparticle (b) and intraparticle (c) phase-separated states (LFP (green) and FP (red)) that occur at small currents and after a current stimulus, respectively, obtained from cells #2 and #3.

and nonaggregated particles was extracted for the preparation of the electrodes used in the microscopy experiments. Particularly, most of the particles in our STEM-EELS study had thicknesses in the range of 70–130 nm, corresponding to a relative thickness (t/λ) close to 1 (here, t and λ are the thickness and mean free path, respectively), thus enabling a reliable collection of EELS spectra (for more details, see Supporting Information Section S2.3). We performed STEM-EELS analysis on particles that had been subjected to a (very) small lithiation current ($-C/100$, Figure 1b), as well as on particles from the experiment involving a high-current stimulus ($-5C$, Figure 1c). In both cases, the corresponding electrodes were at a depth of discharge (DOD) of 0.5, and were obtained from cells #2 and #3 (see Figure S7 in Supporting Information). The details for obtaining the reference spectra for Fe^{3+} and Fe^{2+} , as well as the coordination of the LFP/FP phase map, are described in the SI (Figures S8–S12 and Figure S13, Supporting Information, respectively).

In the context of the current study, the most important finding obtained using STEM-EELS analysis can be understood by comparing Figure 1b,c. We can see that the application of a high-current stimulus results in a significant increase in the number of LFP particles that exhibit intraparticle phase separation (the central part of Figure 1c). This crucial finding directly supports the thermodynamics-based description of the finite-rate phenomenon entering the voltage (energy) hysteresis, as discussed in detail. To some extent, this finding can be anticipated from the large body of experimental evidence using various approaches reported in the field. However, this is the first study to offer systematic and direct evidence that intraparticle phase separation is a consequence of high-current stimuli. Furthermore, a detailed analysis of the level of $\text{Fe}^{2+}/\text{Fe}^{3+}$ mixing in the LFP and FP phases (Section S2.5, Supporting Information), especially the degree of $\text{Fe}^{2+}/\text{Fe}^{3+}$ mixing at the intraparticle LFP/FP phase boundaries obtained from EELS mappings of high-current-activated LFP particles (Section S2.7, Supporting Information), reveals that the degree of local $\text{Fe}^{2+}/\text{Fe}^{3+}$ mixing within the particles is very low. Therefore, the results of the current study strongly suggest that for the high-rate performance of phase-separating insertion materials, the presence of large amounts (fractions) of nonequilibrium phases is not mandatory. Our findings suggest that the presence of the solid-solution Li_xFePO_4 phase(s) is probably not the reason for the high rate performance of the LFP material. Rather, the observed solid-solution phase(s) correspond to a part of the LFP material that has not yet completely relaxed into the corresponding Li-rich and Li-poor phases. This hypothesis, which is a part of our ongoing study, requires more definitive experimental proof(s).

The systematic connection between the electrochemical output and microscopic observations can be better understood via the schemes shown in Figure 1a. Within the hysteretic area, the majority of active particles are in an intraparticle phase-separated state, which does not occur upon regular constant cycling at low C rates.

The phenomenon of interparticle phase separation was experimentally observed in a recent study,^[11] whereas the current study presents and explains the corresponding electrochemical signature of the intraparticle phase-separated state for the first time. The entry into the intraparticle phase-separated state after a preceding high-current excitation regime is a general phenomenon

that can be demonstrated for several phase-transition battery materials and the conditions of interest. We have performed the following sets of diverse experiments, all of which demonstrate entering into a hysteretic loop: i) at different lithiation levels of the electrode (Figure 1 and Figure 2), ii) for current stimuli of different lengths or transferred charge (Figure 2a), iii) different magnitudes of current stimuli at a small base current (Figure 2b), iv) during charge and discharge (Figure S1, Supporting Information), v) at various electrode thicknesses/loadings (Figure 1, Figure 2, and Section S1, Supporting Information), (vi) for different dilution ratios of active material in the electrodes (Figures 2a and S2, Supporting Information), vii) for different phase separating materials (LMP: Figures S5 and S6, Supporting Information) and, finally, viii) entering into hysteretic loop was also demonstrated on commercial cells (Figures S3 and S4, Supporting Information).

As shown in Figure 1a (and even more so in Figure 2a), it is possible to reach voltages very close to the middle of the hysteretic loop. Another general observation is that the voltage remains inside the usual hysteretic loop for a considerable period, more or less almost to the end of the ongoing half-cycle performed at small currents. This phenomenon, which is based on fundamentally different underlying microscopic processes compared to the previously reported phenomena associated with the so-called “memory effect”^[16] and “group-by-group” multiparticle Li battery intercalation^[7,12] (Section S3, Supporting Information), features a large monotonous deviation of the cell voltage.

Figure 2a also indicates that voltage hysteresis occurs during a low discharge current period for very different lengths (durations) of current stimuli, that is, in the range from $\Delta\text{DOD} = 0.008$ to 0.5, confirming that a very short current stimulus is sufficient to enter the hysteresis. A detailed study of Figure 2a further reveals that the voltage approaches the equilibrium value in the case of longer current stimuli (as explained in more detail in Section S1.1.3, Supporting Information). It is also important to emphasize that the experiments presented in Figure 2a were performed on the diluted electrode, which further indicates that ionic and electronic wiring do not affect the key phenomena leading to hysteresis. In addition, Figure 2b shows the entrance into the voltage hysteresis for a wide range of magnitudes of current stimuli and suggests that a deep entrance in the voltage hysteresis is already observed for current stimulus as low as $-C/20$ at a base current of $-C/100$. These cases indicate that when restoring the base current, the potential of the electrode is higher after a current stimulus compared to the potential level at the same base current without a current stimulus. In addition, at the same base current, the electrode potential after a current stimulus is higher than the electrode potential before the current stimulus, despite the higher DOD of the electrode (denoted as the voltage increase after a current stimulus— ΔV , see Figure 2), which tends to lower the electrode potential. These are clear indications that the state of the material was changed by the application of the current stimulus, which will be discussed in more detail later.

Thus far, we have shown the possibility of entering hysteresis at very low base currents. We further demonstrated that the different nonequilibrium states of the phase-separating material at the same bulk lithiation level and temperature significantly influenced the electrochemical characteristics of the battery in the entire operating region, that is, outside the hysteretic

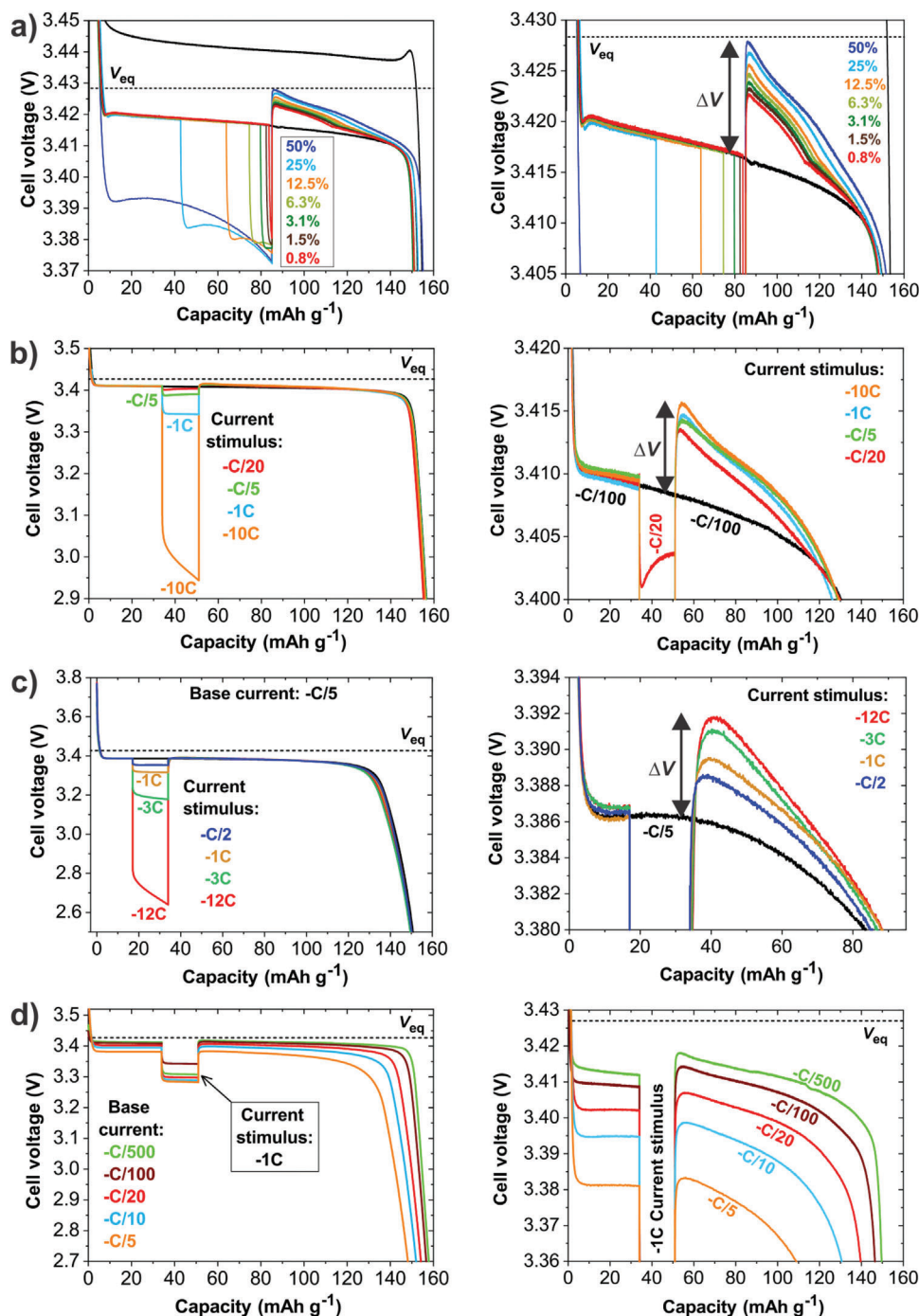


Figure 2. a–d) Voltage increase after a current stimulus for: a) variation of the duration of current stimuli in a wide range of values, i.e., in the range from $\Delta\text{DOD} = 0.008$ to 0.5 (a diluted LFP cathode in cell #11 was used for this set of experiments); b) variation of the magnitudes of the current stimuli in the range from $-C/20$ up to $10C$ at base discharge current $-C/100$ on the LFP-Li cell #8; c) variation of the magnitudes of the current stimuli in the range from $-C/2$ up to $-12C$ at base discharge current $-C/5$ on the LFP-Li cell #8; and d) variation of the base current in the range from $-C/500$ up to $-C/5$ at current stimulus $-1C$ on the LFP-Li cell #8.

loop (Figures 2c,d, and 4). This is demonstrated in Figure 2c, where the altered electric response of the electrode after a current stimulus and its subsequent entry into the intraparticle phase-separated state, is demonstrated for a base current of $-C/5$. Figure 2d shows an increased cell voltage after the application

of a current stimulus and the restoration of the same base current for a wide range of base currents. The results presented in Figures 1 and 2, and in Section S1, Supporting Information, confirm the generality of the altered electric response of the electrode in the intraparticle phase-separated state under a wide range of

dynamic operating conditions. This has far-reaching and general material-related consequences as it positively answers a material-related question by demonstrating that the phase-separating material in the electrode can feature (significantly) different potentials at the same bulk lithiation level and temperature when exposed to the same finite current. We note that the variation (reproducibility) of the voltage curves measured during the baseline low-current regime measurements is $\approx \pm 0.5$ mV (in a thermostat with a controlled temperature at 25.0 ± 0.1 °C). The apparent omnipresence and importance of the present phenomenon may raise another question: why has the possibility of entering the intraparticle phase-separated state not been previously reported? The answer may be partially linked to the absence of targeted and systematic electrochemical and microscopic experiments, as presented in Figure 1. However, this phenomenon might have been overlooked. The entrance into the intraparticle phase-separated state is associated with relatively small potential differences compared to other phenomena influencing overpotentials; however, the effects are far from negligible in practice, as discussed in Section 2.5. Nevertheless, as seen from the systematic studies shown in Figure 2 and Figures S3–S8, Supporting Information, there is a clear and reproducible electrochemical signature of entering the intraparticle phase-separated state over a very broad range of base currents and current stimuli. This signature was observed even though some of the voltage levels after current stimuli did not enter into hysteresis owing to high overpotentials (Figure 2c,d). It is also important to note that the smallest current stimulus required to enter the intraparticle phase-separated state was much smaller than the largest base current used in this study (Figure 2).

These additional pieces of evidence, combined with previous arguments on the generality of the observed phenomenon (Figure 1 and Figure 2, Section S1, Supporting Information) under a wide range of dynamic operating conditions, strongly suggest that at least a non-negligible share of active particles enter and remain in the intraparticle phase-separated state during the realistic dynamic operation of a battery (Figure 3c,e). However, as is discernible from the present figures and accompanying explanations, a very large proportion of active particles can enter the intraparticle phase-separated state after larger current stimuli, which at low base currents results in a very deep entrance into the voltage hysteresis, approaching the middle of the hysteretic loop (Figures 1 and 2a).

2.2. Theoretical Background

In idealized diluted and homogeneous electrodes with identical particles, the intraparticle phase-separated state represents an ensemble of particles, all of which are split uniformly into two phases occupying equal volumes within each particle if the DOD is 0.5. In a more realistic situation, where the distribution of particle properties and their heterogeneous ion and electron wiring are considered, one may expect a distribution of the degree of particle lithiation, as schematically depicted in Figure 1a (central scheme). This scheme is well supported by experimental observations using STEM-EELS (Figure 1c), in which several particles are split into two phases, although each particle has a slightly different degree of lithiation (for details, see Section S2, Supporting Information). In any case, the intraparticle phase sep-

aration differs from the interparticle phase separation, which is experimentally shown in Figure 1b. This occurs at small currents without applying current stimuli, further supporting the postulation of a particle-by-particle lithiation process at low currents.^[10] Because the intraparticle phase-separated state exhibits a lower chemical potential, it is characterized by a higher potential of the bulk active material and thus of the electrode with respect to the other known states of the active material, as shown in Figures 1a, Figure 3, and Figure 4.

The thermodynamic basis for the present explanation relies on the postulate that the lithiation level of the electrode is equal to the sum of the Li mole fractions of the many-particle system q ^[10]

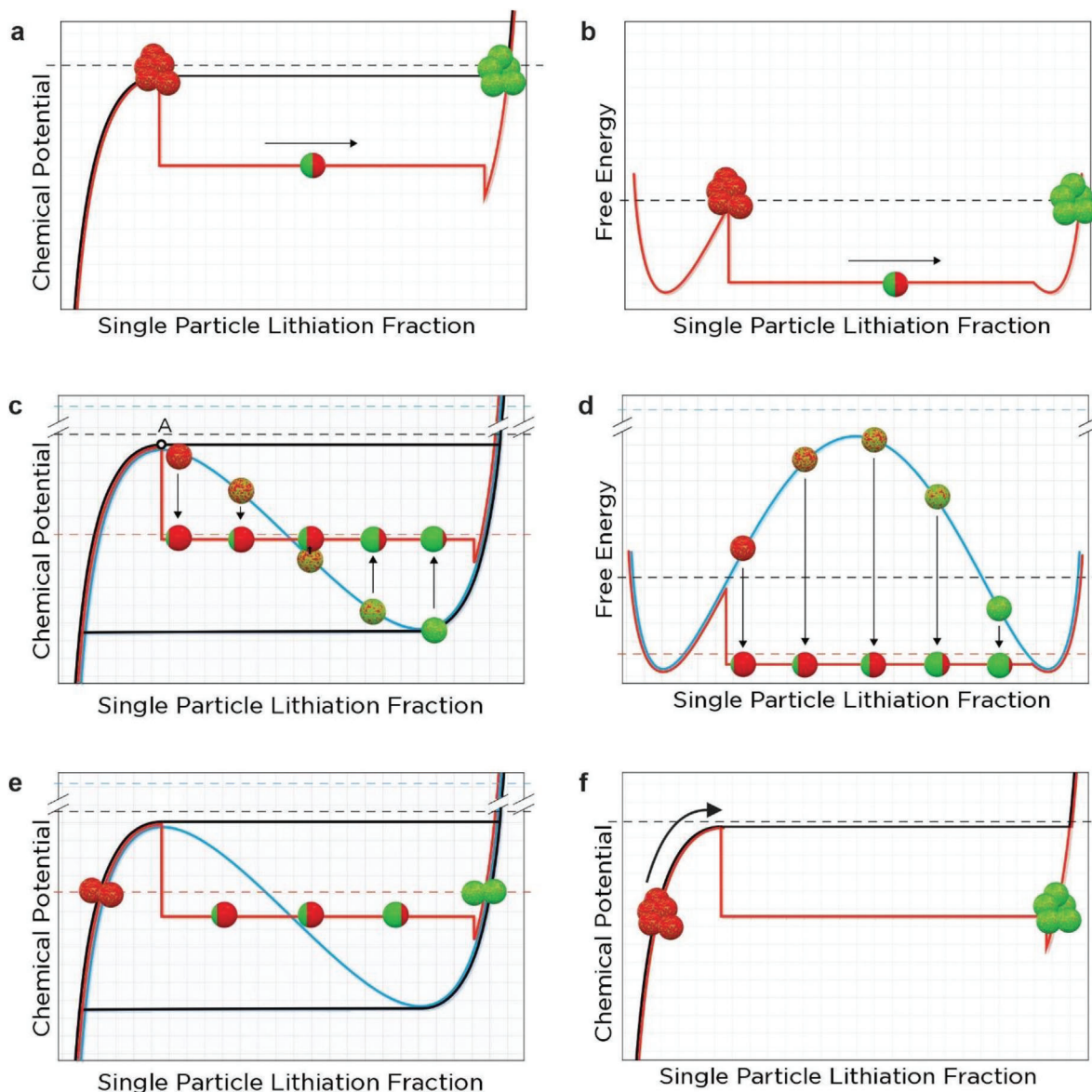
$$q = \frac{1}{N} \sum_{l=1}^N x_l, \quad (1)$$

where x_l is the Li mole fraction of an individual particle (indexed by l), and N is the number of (de)lithiating particles inside the electrode. This constraint implies that in a many-particle system, it is only possible to control the total amount of Li in all the particles; thus, the amount of Li inside the individual particles is not uniquely determined. Another driving force for this behavior is the free-energy minimization of the many-particle system.

$$F_{\text{TOT}} = \sum_{l=1}^N \left[\int_{V_l} f_l(x_l) dV \right] \quad (2)$$

where F_{TOT} denotes the total free energy of the many-particle system, V_{ll} and f_{ll} are the volume and free-energy density of an individual particle, respectively. The amount of lithium inside individual particles (x_{ll}) and the exchange of lithium among active particles are therefore driven by the minimization of the energy of the whole ensemble.

This thermodynamic basis offers a direct explanation for all the states depicted in Figure 1 (see also Section S4, Supporting Information). At small currents and consequent small overpotentials that barely exceed the initial energy barrier imposed by the convex part of the free energy density of a particle (Figure 3a,b), the particles undergo interparticle phase separation. During most of the (dis)charge cycle, the vast majority of particles are at high and low lithiation levels.^[10,34] In contrast to the intraparticle phase-separated state, the interparticle phase separation is characterized by the particle-by-particle lithiation regime (Figure 3a,b), where only a small fraction of particles is simultaneously active (ref.[10] and Figure 5b), which forms a mosaic pattern of particles^[10] (see also Figure 1b). This is also supported by Figures 3b,d, and S29d, Supporting Information, which present corresponding representations in the free energy diagram showing insufficiently high energy for particles to transverse the lithiation range in the high-overpotential transient regime. The resulting inter-particle phase-separated state inherently yields voltage hysteresis.^[10] This phenomenon is schematically presented in Figure 3a,f. Figure 3f shows the interparticle phase-separated state at the mid-levels of the DOD under equilibrium conditions, that is, during a long period of zero current. In this case, the active particles undergo phase separation, such that some particles are lithiated and some are delithiated,



	Chemical potential	Overpotential
High overpotential transition state	— (solid blue)	- - - - (dashed blue)
Interparticle phase separated state	— (solid black)	- - - - (dashed black)
Intraparticle phase separated state	— (solid red)	- - - - (dashed red)

Figure 3. a) Schematic presentation of constant small current discharge, without a previous current stimulus, corresponding to interparticle phase-separated state, being characterized by particle-by-particle lithiation process and b) corresponding representation in the free energy diagram. In this case, the chemical potential of the electrode is above the spinodal point, as indicated by the black dashed line. c,d) Schematic presentation of chemical potential (c) and free energy (d) during entering intraparticle phase-separated state. Under the application of a larger current, the majority (or significant share) of the active particle population undergoes a nonequilibrium transition following the spinodal potential, which, as elaborated in Section S3.2, Supporting Information, indicates a high-overpotential transient state. After a sufficiently fast reduction of a current, and thus, the overpotential, the majority of particles undergo intraparticle phase separation (i.e., they internally split into two phases) yielding the intraparticle phase-separated electrode state. The chemical potential of the particle in the intraparticle phase-separated state is close to the equilibrium state (red dashed line in (c)) and is characterized by a minor offset of the free energy associated with intraparticle strain and interfacial energy due to the internal phase boundary.^[44] e) If current stimuli are smaller or shorter or if the base current is larger, the share of particles in the intraparticle phase-separated state is lower, which results in the increased chemical potential of the bulk active material. f) Schematic representation of the interparticle phase-separated state in equilibrium conditions at mid-levels of DOD, where particles do phase separate in a way that some particles are lithiated and some delithiated. The arrow indicates an initial increase of the chemical potential required to surpass the chemical potential barrier at the application of a finite current.

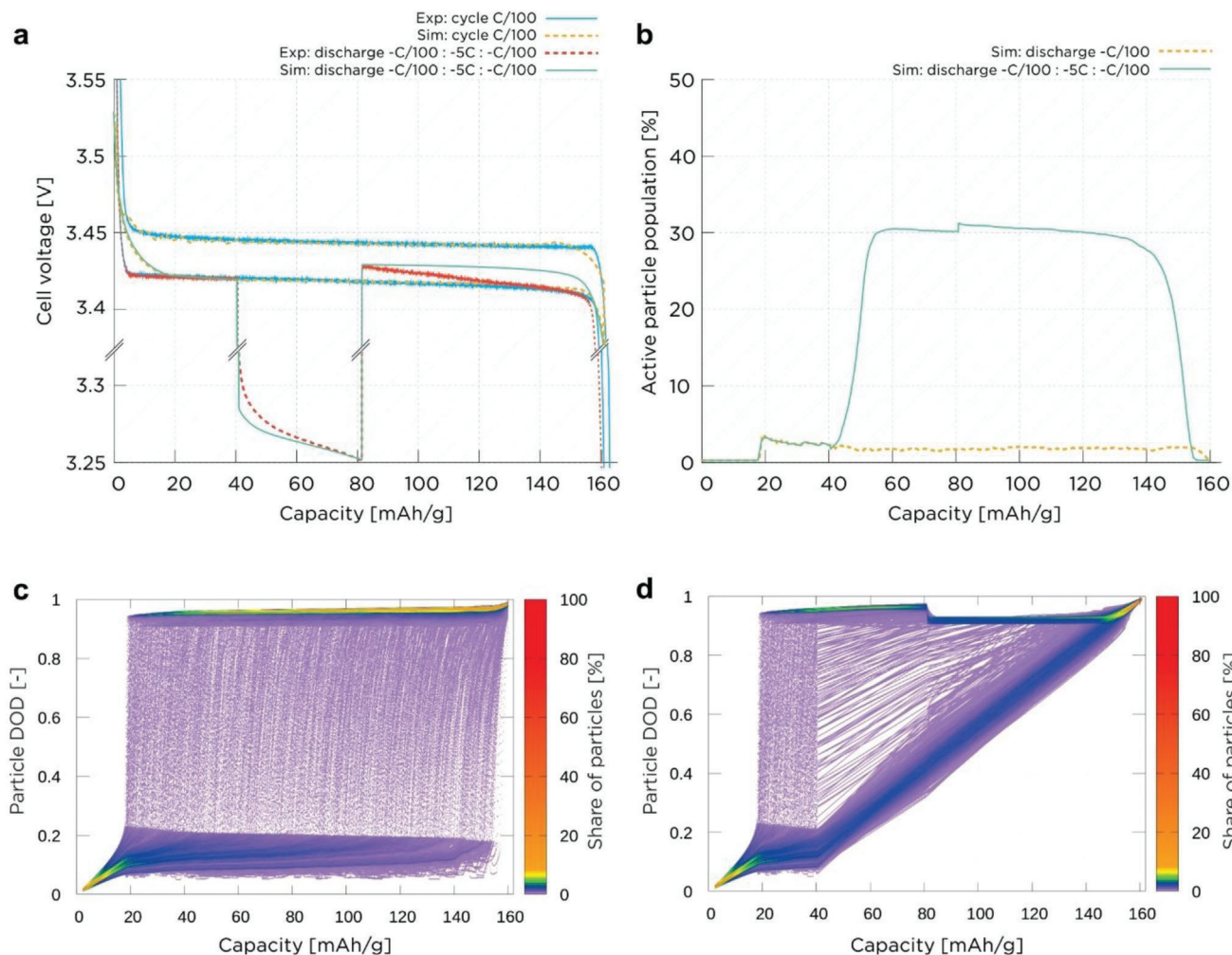


Figure 5. a) Comparison between experimental (cell #1) and simulation results for hysteresis obtained at C/100 charge and discharge cycle as well as for $-C/100$ discharge with a $-5C$ discharge stimulus between 25% and 50% DOD (discharge $-C/100 - 5C - C/100$). b) Simulated active particle population for $-C/100$ discharge and $-C/100$ discharge with a $-5C$ discharge stimulus between 25% and 50% DOD. c,d) Evolution of the DODs of the particle as a function of the electrode level or cell capacity during discharge. The initial solid solution lithiation until the spinodal point followed by particle-by-particle lithiation lasting nearly to the end of the cell capacity range is shown in (c). (d) clearly shows the initial solid solution lithiation until the spinodal point followed by particle-by-particle lithiation until 25% DOD and subsequent lithiation in the high-overpotential transient state increasing active particle population, also shown in (b). This is a prerequisite for entering the intraparticle phase-separated state upon reduction of the current. This intraparticle phase-separated state is characterized by a larger share of active particle population at high potentials ((b) and (d)) further supporting key conditions that need to be satisfied to enter into the hysteretic loop under dynamic operating conditions.

and their chemical potential is approximately in the middle of the hysteresis (Figure 3f and Section S5, Supporting Information). The arrow in Figure 3f indicates the increase in the chemical potential required to surpass the chemical potential barrier upon the application of a finite current, resulting in an intraparticle phase-separated state at a higher chemical potential (Figure 3a). The higher chemical potential of the interparticle phase-separated state, which decreases the cell voltage, is the origin of the voltage hysteresis that occurs during the discharge/charge cycle at small currents. Despite the small currents, this hysteresis is characterized by non-negligible entropy generation, resulting in the dissipation of useful electrochemical work such as heat.^[17] To a large extent, this is a consequence of the chemical potential barrier that imposes states on the system that are far from

thermodynamic equilibrium and Li redistribution between the particles.^[10]

Another limiting (dis)charging regime is observed at large currents when the system is far from thermodynamic equilibrium and is thus characterized by high overpotentials. In that regime, the majority of particles simultaneously lithiated via a pathway involving a poorly defined, nonequilibrium disordered structure denoted as the “high-overpotential transient state” (Figure S29c,d, Supporting Information), and this has been confirmed by multiple simulations and experimental studies.^[15,39–42] This high-overpotential transient state is characterized by a large active particle population.^[11,34,42]

The thermodynamic background explaining the dynamic protocols for entering the intraparticle phase-separated state is

graphically shown in Figure 3c,d. The following key conditions for entering the intraparticle phase were identified:

- The application of a current stimulus that is sufficiently larger than the base current and ends inside the spinodal region ensures that a considerable share of the active particle population undergoes a transition through a high-overpotential transient state (Figure 3c,d).
- A sufficiently fast reduction of the current to a sufficiently low value so that local overpotentials are appropriately reduced results in the phase separation of particles in the high-overpotential transient state.
- Simultaneously, the minimization of the energy of the entire ensemble (Equation 2), driving the intraparticle and interparticle redistribution of lithium with a preferential occurrence of intraparticle phase separation (Figure 3c,d) over interparticle phase separation owing to longer characteristic times for the latter.^[11]
- Entering the intraparticle phase-separated electrode state, where the majority (Figure 3c, or a significant share, Figure 3e) of the particle population is intraparticle phase-separated, is characterized by a lower energy level, and therefore, by a lower intraparticle phase-separated chemical potential compared to the interparticle phase-separated chemical potential, increasing the electrode potential.

There is an additional condition for entering into the hysteretic loop:

- The base current should be sufficiently low such that the overpotentials after the current stimulus are smaller than the electrode potential increase associated with the intraparticle phase-separated state.

The existence and interplay between intraparticle and interparticle phase separation have been investigated in several experimental studies.^[35,41,45–47] Detailed reasoning on the different characteristic times for intraparticle and interparticle phase separation is provided in Section S5, Supporting Information. This detailed reasoning addresses the causal chain of phenomena that covers the transition from the high-overpotential transient state to the long-term-lived intraparticle phase-separated state and subsequent relaxation to the lower energy interparticle phase-separated state with long characteristic times.

Figure 2 and Figure 4c indicate that the voltage increases after current stimuli, which are associated with the share of particles in the intraparticle phase-separated state, are not identical for different combinations of base currents and current stimuli. In addition, the duration of the stimuli also exerts an effect. These phenomena can be schematically explained by comparing Figure 3c,e. Figure 3c shows a limiting (hypothetical) case, in which all active particles would enter the intraparticle phase-separated state. In this case, the potential of the active material that has been exposed to a small current (denoted as the nonequilibrium active material potential) approaches the open-circuit potential of this material at a given level of bulk lithiation. Therefore, at low currents, the electrode potential deeply enters into the voltage hysteresis because of the overpotentials due to the reaction kinetics. Moreover, the transport phenomena are neg-

ligible (Figure 4b). However, Figure 2 also reveals that the voltage increase after current stimuli can be smaller if the current stimuli are smaller or shorter or if the base current is larger (e.g., approaching 1C, Figure 4c). In these cases, fewer particles entered the intraparticle phase-separated state, as schematically depicted in Figure 3e. Consequently, the intraparticle phase-separated state with a lower proportion of active particles features an increased chemical potential of the active material compared to the intraparticle phase-separated state with a higher proportion of active particles, which inherently yields a lower nonequilibrium potential of the active material (Figure 4b) and a lower cell voltage. This explains the different voltage increases after the current stimuli, as presented in Figure 2.

The theoretical findings are summarized in Figure 4. A large difference is observed in the electrode potentials of the interparticle and intraparticle phase-separated states at very small currents (Figures 1a and 4a). This can be explained by the fact that the voltage hysteresis originates from two contributions: i) a potential shift owing to a nonequilibrium active material potential ($\Delta\Phi_{AM,neAMne}$), since a large share of particles is at the lithiation level that corresponds to the first spinodal point (Figure 3a), and ii) overpotentials owing to reaction kinetics and transport phenomena (η) (Figure 4b). Both contributions yielded half of the total hysteresis observed during the full cycle, $V_{hh}/2$. When entering the intraparticle phase-separated state, $V_{hh}/2$ almost completely vanishes when the proportion of active particles is very large (Figure 4b). This is a consequence of two contributions. The first is a nearly eliminated shift due to the nonequilibrium active material potential ($\Delta\Phi_{AM,neAMne}$) because intraparticle phase-separated particles have a lower chemical potential (Figure 3c). The second contribution arises from the lowered overpotentials owing to a larger share of the active particle population in the intraparticle phase-separated state, thereby reducing the losses associated with the reaction kinetics and transport phenomena. Consequently, the intraparticle phase-separated state is associated with a much lower $V_{hh}/2$ than the interparticle phase-separated state, which leads to the voltage increase after current stimuli denoted by ΔV . To support the reasoning behind the results presented in Figure 2, Figure 4b presents two cases of an intraparticle phase-separated material with a lower (Figure 3e) and larger (Figure 3c) proportion of active particles, resulting in different values of $V_{hh}/2$, whereas both are smaller than the $V_{hh}/2$ value of the interparticle phase-separated state. Figure 4c shows the ΔV values for all cases presented in Figure 2 further supporting the finding that a phase-separating material in the electrode can feature (significantly) different potentials at the same bulk lithiation level and temperature when exposed to the same finite current. Hence, Figure 4 represents a theory-based bridge between the macroscopic electrochemistry and microscopic processes analyzed in Section 2.1.

2.3. Simulation Results

The thermodynamic explanation proposed in the previous section is further supported by simulation results obtained with the extended continuum-level porous electrode model^[48] shown in Figure 5 and discussed in detail in Sections S6.1 and S6.2, Supporting Information. The advantages and limitations of the

proposed model are discussed in detail in the next section. It is important to note that all key phenomena of entering the intraparticle phase-separated state are confirmed by tailored experimental techniques and that the modeling of all relevant phenomena in multiparticle electrodes exhibiting collective effects is beyond the current capabilities. Therefore, a simulation model was applied to provide a provisional link between the thermodynamic reasoning presented in Figure 3 and the experimental evidence presented in Figure 1, to elucidate the thermodynamic background of the newly discovered phenomenon without claiming a full quantitative agreement. Nevertheless, the model replicated the $C/100$ hysteresis with acceptable accuracy. Importantly, it is capable of predicting the entrance into hysteresis when entering the intraparticle phase-separated state upon the reduction of the current after the current stimulus. An adequate model prediction of ΔV after the current stimulus, Figure 5a, was the Primary aim of applying the simulation model. Therefore, the present simulation results establish a model-based bridge between thermodynamic reasoning (Section 2.2) and experimental evidence (Section 2.1). Figure 5a also reveals that the discrepancies between experimental and simulation results become observable after adequately predicting voltage increase after current stimuli, i.e., ΔV . This can be attributed to a very complex interplay of phenomena, which cannot yet be adequately captured to the full extent in multiparticle models aimed at simulating hundreds of hours of battery operation, as explained in Section S6.1, Supporting Information. Nevertheless, at 50% DOD, Figure 5b–d show that, in the small current regime, the active particle population is significantly larger at the same level of electrode lithiation when a current stimulus is applied, which is in agreement with experimental findings. Therefore, the combination of a significantly increased active particle population and a higher cell voltage (Figure 5a) provides unique proof of the hypothesis on the simultaneous entrance of a larger share of the active particle population into the intraparticle phase-separated state after a large current stimulus (more details are provided in Section S6.2, Supporting Information). Therefore, both parameters can only be achieved simultaneously if the electrode is in the intraparticle phase-separated state. This is because a higher battery voltage can only be realized if a large share of the particles feature lower chemical potentials, such as those inherently found in particles that are in the intraparticle phase-separated state. This agrees with the thermodynamic reasoning shown in Figure 3.

2.4. Further Experimental Evidence

This section presents additional electrochemical results that further underline the impact of this newly discovered phenomenon on the electrical output of the cell. **Figure 6c,d** offer direct experimental proof that after applying a current stimulus of $-3C$ the cells exhibit considerably different electrochemical characteristics compared to a nominally identical cell discharged at $-C/30$ (Figure 6b) within the same initial DOD range (from 0 to 0.1). The significantly different current responses (Figure 6c), as well as the different ratios of the apparent cell-level total (DC) resistances (Figure 6c) of both cells, confirm that after a current stimulus, the electrode enters a different state, that is, intraparticle phase separation. The macroscopically observed significant vari-

ation in the apparent DC cell resistance after a current stimulus was directly related to the higher potential level of the intraparticle phase-separated electrode state (Figures 1a and 3a) and the lower overpotential for lithiation owing to a larger share of the active particle population (Figure 4). Importantly, after the cells were connected in parallel (inset of Figure 6b), the voltages of both cells increased, which is consistent with the findings in Figure 1 and Figure 5 as well as with the thermodynamic reasoning presented in Figure 3. As expected, the trends of the current and resistance ratios are reversed towards the end of the discharge period (Figure 6c,d), as the present cells feature nominally identical capacities.

The connection between a lower overpotential for lithiation and a larger proportion of the active particle population can be explained thermodynamically, as depicted in **Figure 7a,b**. During a small current discharge, a large proportion of the particles are at the lithiation level, which corresponds to the first spinodal point (Figure 7a). This is characterized by a large derivative of free energy, ΔF_1 (i.e., potential), as a function of variation of the single particle lithiation fraction (Δc), and consequently, the current (Figure 7a). In contrast, the intraparticle phase-separated state was characterized by a much smaller gradient of free energy, ΔF_2 , as a function of the variation in the single particle lithiation fraction, Δc (Figure 7a), and thus impedance (including DC resistance). From a different perspective, it can be said that the phase boundaries, which are inherently present in intraparticle phase-separated particles, are moved without a large energy penalty.^[44]

Finally, the proposed mechanism was additionally confirmed by other experimental evidence employing electrochemical impedance spectroscopy (EIS) measurements after galvanostatic excitation at different rates ($C/100$ and $5C$), terminated at a DOD of 0.1 (Figure 7c). The experiments show a pronounced effect of the preceding current stimulus on the low-frequency part of the impedance response, in which solid-state or active-material processes strongly prevail. Specifically, after a large current stimulus (red curve), this part reveals impedance values that are 20%–40% lower compared to the case with a small current (blue curve). This different behavior further proves that the intraparticle phase-separated state is characterized by a lower overpotential for lithiation, owing to a larger share of the active particle population being closer to the equilibrium state.

2.5. Discussion

On a broader scale, entering a hysteretic loop has been reported for systems other than stable multiparticles.^[22–25] For example, such states have been achieved by changing the temperature of a multiphase system and tracing the temperature path dependence or shifting the system vertically across the phase lines of the phase diagram. Unlike these previous studies, we have demonstrated and explained the existence of long-living intraparticle phase-separated states, which enable entrance into the hysteretic loop at small base currents, of a phase-separating Li intercalation material by shifting the multiphase system (i.e., phase-separating active particle) horizontally across the phase diagram in the direction of variation in the fraction of lithiation. In addition, we provide clear experimental and theoretical

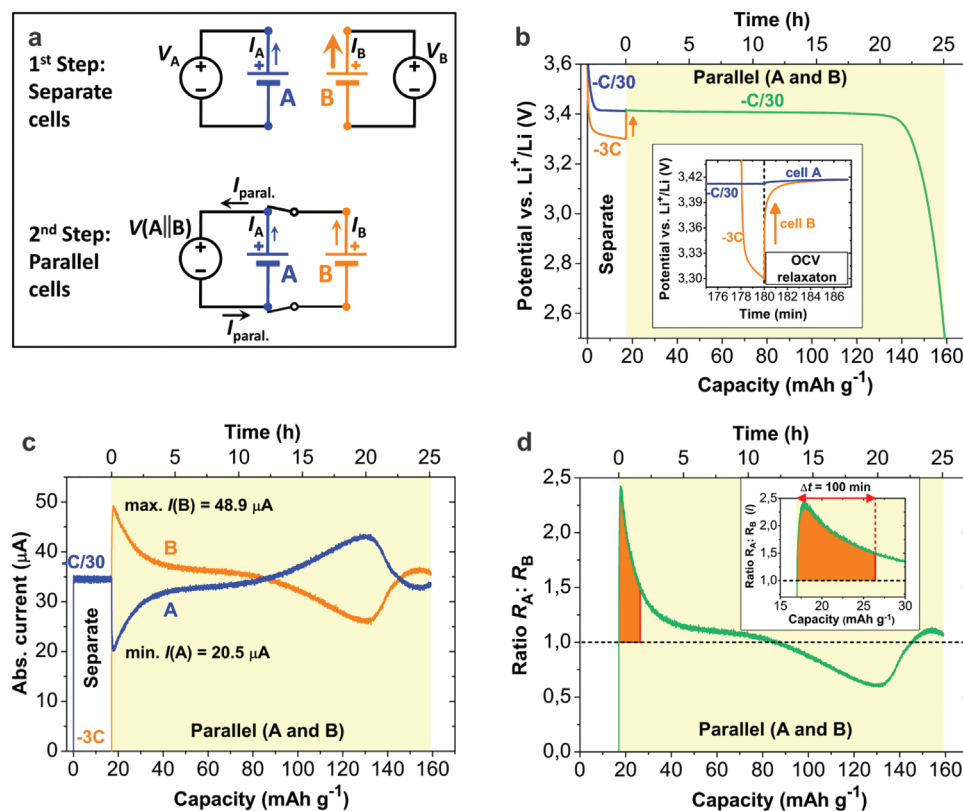


Figure 6. a) Schematic presentation of a parallel battery experiment performed on two nominally identical LFP-Li cells (A = cell #4 and B = cell #5). In the 1st step, each cell was connected to its own current (voltage) source with the corresponding terminal voltages V_A and V_B . During the following 2nd step the cells were connected in parallel to a single current (voltage) source with a terminal voltage $V(A||B)$. b) During the 1st step, the cells were partially galvanostatically discharged whereby their global DOD was changed from 0 to 0.1; however, the magnitude of discharge current was different: $-C/30$ for cell A (blue curve) and $-3C$ for cell B (orange curve). The discharge was followed by a short relaxation period at the open circuit (inset in (b)). In the 2nd step, the cells were connected in parallel (A||B, green curve in (b)). While the pair was discharged using a total current of $-C/30$, the individual currents through the cells (I_A and I_B) were also monitored. c) A strong deviation of the individual cell currents from the total current value $-C/30$ is observed. Importantly, in the initial part of the 2nd step, a considerably larger current is observed in cell B which in the 1st step was subjected to a larger current ($-3C$). d) The observed effect can be expressed in terms of the ratio of the apparent DC cell resistances $R_A:R_B$, where the maximal value of the ratio was found to be as large as 2.4. The zero value on the time scale corresponds to the end of the current stimulus.

evidence that the system remains in the intraparticle phase-separated state, and thus, at a higher electrode potential under nonequilibrium conditions, that is, at a range of finite currents.

Moreover, the higher potential level of the electrode and higher share of active particles inherent to the intraparticle phase-separated state (Figure 1a and Figure 3a) also explain why parallelly connected cells of the same type feature significantly different currents despite being at the same DOD and temperature (Figure 6). In addition, the intraparticle phase-separated state is characterized by a much smaller gradient of free energy as a function of the variation in the single particle lithiation fraction (Figure 7a) and a larger share of the active particle population. These particular characteristics of the intraparticle phase-separated state explain why cells at the same DOD and temperature feature a much lower impedance in the low-frequency part of the impedance response, in which solid-state processes strongly prevail (Figure 7c). These findings are of overarching importance not only for a better understanding of the fundamental processes occurring in state-of-the-art battery systems but also for their increased control, diagnostics, and monitoring during dynamic battery operation in real applications.

In this context, it is to be noted that the levels of the base currents and stimuli presented in Figure 2 and Section S1, Supporting Information, cover a realistic range of currents encountered in several applications. Despite the relatively small voltage shifts owing to the intraparticle phase-separated state, such changes are significant. For example, in an LFP-based electrode, the entrance into the intraparticle phase-separated state yields a voltage shift of up to 10 mV (at any given DOD) with respect to the value observed at the same DOD under normal (low current) operation of the cell (Figure 2, Figure 4, and Sections S1.1 and S1.2, Supporting Information). In the case of LMP active materials, this shift can reach up to 20 mV (Section S1.3, Supporting Information). These values were significantly larger than the typical slopes of the open-circuit potentials (OCP) of phase-separating materials. Specifically, in the region within the spinodal points, the present Targray material features an open-circuit potential (OCP) slope of $\approx -1 \text{ mV}$ for the ΔDOD of 10%. Similarly, a pure LTO material^[7] exhibits a pseudo-OCP slope (measured at small currents) of less than -0.5 mV for ΔDOD of 10%, whereas another reference^[49] also shows a pseudo-OCP slope in the range of -0.5 mV for ΔDOD of 10% for an LFP/LTO cell. Since graphite also features

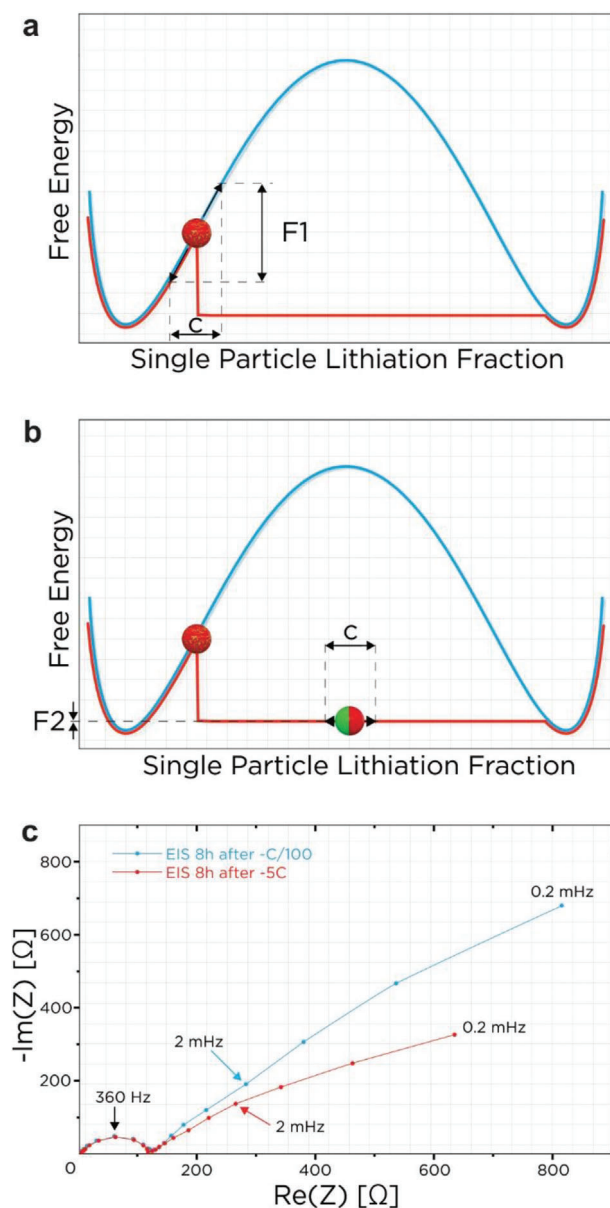


Figure 7. a) Schematic explanation of larger impedance of the interparticle phase-separated state compared to b) the intraparticle phase-separated state indicating smaller gradient of free energy (f) and thus potential as a function of variation of the single particle lithiation fraction (c); the color code in (a) and (b) is identical to that in Figure 3. c) EIS measurements of the experimental cell #6 measured 8 h after the termination of 5C discharge at DOD 0.1 (red curve) and after the termination of C/100 discharge at DOD 0.1 (blue curve).

a very flat OCP region with ≈ -0.7 mV for ΔDOD of 10%,^[50] the voltage shift due to entering the intraparticle phase-separated state (ΔV) features much higher values compared to OCP variation for the significant values of DOD. The values of ΔV are also much larger compared to the maximum cell voltage error of voltage sensors for battery management systems featuring values of 1 mV or even less with cell voltage measurement resolution in the range of 0.1 mV or up to a few tenths of a millivolt.^[51–53] In the light of these typical practical numbers that are within

or below the voltage shifts related to the present discovery, it is reasonable to assume that the discovery will ultimately push the boundaries of understanding for advancing the control, diagnostics, and monitoring of batteries composed of phase-separating materials.

Ultimately, inspired by the newly revealed causal chain of events in phase-separating materials, the battery community may try to search for new ways of minimizing entropy generation in future electrode designs and/or with the elaboration of tailored control strategies for batteries and battery systems by exploring the interactions between material properties, particle size-dependent effects,^[54,55] the impact of particle connectivity^[48,56] and current profiles. In particular, if a battery could predominantly operate in the intraparticle phase-separated state, it would exhibit very low losses, and thus minimize heat generation.

3. Conclusions

In terms of scientific progress, this study provides a comprehensive resolution to the fundamental question of whether a phase-separating material can feature (significantly) higher potentials at the same bulk lithiation level and temperature when exposed to the same finite current. This was achieved by linking the electrochemical experiments to an accurate microscopic analysis (STEM-EELS), which enabled the revealing of the electrochemical signature of the intraparticle phase-separated state (two different phases occurred within most of the individual active particles). Importantly, the intraparticle phase-separated state is characterized by a higher potential for the active material than the interparticle phase-separated state at the same bulk lithiation level and temperature when exposed to the same finite (low) current. In addition, we unambiguously show that the entrance into the intraparticle phase separated after a preceding high-current excitation regime is a general phenomenon that can be demonstrated for several phase-transition battery materials and conditions of interest. This was demonstrated through experiments conducted on different phase-separating active-battery materials under different dynamic conditions. It was shown that a high(er) C-rate operation increases the share of particles in the intraparticle phase-separated state. In contrast, at low C-rates, the transition to the intraparticle phase-separated state is negligible. The intraparticle-separated state exhibits voltage increases in the range of 10 mV for LFP-based electrodes, whereas, for their LMP-based counterparts, the voltage increases can exceed 20 mV. Importantly, once formed, the intraparticle phase-separated state can persist for several hours within the electrode, thereby affecting the voltage. This can be summarized as a fundamental explanation of the origin of the dependency of electrode potentials for phase-separating materials, as from the current findings it is evident that the history of battery charging-discharging dynamics will have a decisive impact on the actual potential of phase-separating electrode materials at any given moment. These findings also explain the apparent “breach of thermodynamic postulates” by entering the hysteretic loop at sufficiently low finite currents. It can be envisaged that this newly discovered phenomenon will have far-reaching consequences in the technological applications of batteries (such as diagnostics, monitoring, and control), where state-of-the-art devices exploit voltage changes in the range of 1 mV or even less.

4. Experimental Procedures

4.1. Active Cathode Materials

Three types of LiFePO_4 (LFP) battery-grade powder materials were used as active materials for the LFP cathodes. a) Commercially available powder provided by Targray (SLFP02002): according to the specifications, this LFP material has a specific surface area of $11 \pm 2 \text{ m}^2 \text{ g}^{-1}$, an agglomerate size of $3 \pm 1 \mu\text{m}$ by the D50 criterion and a native carbon content of $2 \pm 1 \text{ wt}\%$. b) The second type of LFP material was prepared using a novel pulse combustion reactor (PCR-method) method in a slightly reductive environment, as described in detail in our previous paper.^[57] However, extensive experiments did not reveal any meaningful effect of the synthesis procedure on this phenomenon. Briefly, the second material was synthesized in a reactor setup consisting of a Helmholtz-type pulse combustor with a natural frequency of 280 Hz (at a temperature of approximately 1250 K) and a 4 m-long stainless-steel reactor pipe. Air was supplied to the combustor using an aerodynamic valve via a blower. This method allows precise control of the atmosphere in the reactor, as well as the frequency and amplitude of pulses, all of which have a pronounced effect on the reaction outcome.^[58] In the current synthesis, the spraying gas was 99.9% nitrogen, with a pressure of 1.5 bar and a flow of 45 mL min^{-1} . The precursor was composed of 13.5 g of LiNO_3 , 76.1 g of $\text{Fe}(\text{NO}_3)_3 \cdot 9\text{H}_2\text{O}$, 36.4 g of triethyl phosphate, 78.5 g of glycine, 30.9 g of NH_4NO_3 , everything dissolved in 400 g of deionized water. We used a 4 mol.% excess of lithium owing to losses in the reactor and annealing oven. The temperature at 0.5 m after the spray nozzle was maintained at $700 \pm 5 \text{ }^\circ\text{C}$ with the amount of precursor sprayed being $20 \pm 1 \text{ mL min}^{-1}$. The combustion frequency was maintained at 240 Hz. The prepared material was collected in an electrostatic precipitator and annealed in an electrical oven under a constant argon flow and in the presence of carbon at $700 \text{ }^\circ\text{C}$ for 6 h. The annealed material had a tap density of approximately 1 g cm^{-3} and was used as prepared for the preparation of cathodes. c) The third type of LFP material was used specifically for the experiments in which STEM-EELS analysis was performed (Figure 1b,c). The material was essentially a commercial LFP powder provided by Targray and was not exposed to any further chemical modification or heat treatment. To perform STEM-EELS measurements, we selectively removed large agglomerates and the largest LFP aggregates from the starting Targray LFP powder by centrifuging the dispersed Targray LFP powder in an inert organic solvent. 9 g of the starting Targray LFP was dispersed in 300 mL of isopropanol (propan-2-ol), where 70 mg of Triton X-100 (Sigma-Aldrich) non-ionic surfactant was dissolved; the latter was shown to be completely compatible with the LFP cathode.^[59] Ultra-Turrax T25 (IKA) homogenizer was used at 13000 rpm for 30 min to break apart large agglomerates, followed by 20 min of sonication with an ultrasonic liquid horn disperser (Sonics, Vibra-Cell) by applying a sequence of 8 s pulse + 2 s pause steps in a cooling ice bath to promote effective dispersion of particles. We applied the first centrifugation step (5 min at 2300 rpm) to remove large aggregates (settled at the bottom of the centrifuge tube) and a second centrifugation step (30 min at 10000 rpm) to remove the desired fraction of LFP particles from the excess Triton X-100 in the residual solution, the smallest (nano-) particles of LFP and potential impurities that remained

in the dispersion. The sediment of LFP particles was redispersed in fresh isopropanol, and the anticipated powder sample of LFP particles with selected particle size was obtained (150 mg) after final drying under reduced pressure (rotary evaporator, 3 mbar, $40 \text{ }^\circ\text{C}$).

4.2. Electrode Preparation

Conventional porous electrodes were prepared using the standard procedure for preparing laboratory-scale cathodes. Starting from a selected active material (AM) powder and carbon black (CB) conductive additive, we prepared a homogeneous slurry (dispersion) of the solid components in an already prepared 15 mg mL^{-1} solution of PVdF binder (182702 Aldrich) in NMP solvent (99.5% pure, 8.06072.2500 Merck) to obtain the final standard (dry) electrode composite composition AM: CB: PVdF = 90: 5: 5 (wt%). The special (nonstandard) composite formulations used in this study are listed in **Table 1**. The composition of the LMP-based cathodes was AM:CB:PVdF = 80:10:10 (wt%). The slurry was homogenized in a planetary mill for 30 min at 300 rpm and then applied to the surface of a carbon-coated Al foil using an automated doctor blade applicator. The distance between the blade and the surface of the Al foil was set to $200 \mu\text{m}$. In the first step, the coated Al foil was dried for 3 h at $90 \text{ }^\circ\text{C}$ at reduced pressure (10 mbar). Subsequently, we cut circular electrodes with a diameter of 16 mm (geometric area $A = 2 \text{ cm}^2$). The electrodes were pressed by applying 5 t (2.5 tons per 1 cm^2) for 1 min in a hydraulic press. Before transferring to an argon-filled glove box, the electrodes were additionally dried under vacuum overnight at $90 \text{ }^\circ\text{C}$ in a vacuum chamber. This implied the prepared electrodes had typical LFP mass loadings of about 3–4 mg per cm^2 of the electrode geometric area (composite loading 3.3–4.4 mg per cm^2) and the obtained composite thickness was in the range of 18 to $19 \mu\text{m}$. The electrode porosity was calculated by taking the values of the electrode composite mass, thickness, and bulk density of the composite components as 41–44 vol%. The porosity of the LFP cathodes is comparable to the typical practical range of LFP cathodes with good electrochemical performance.^[59,60] The special (dedicated) electrode composite formulations and parameters are presented in **Table 1**.

4.3. Preparation of Electrochemical Cells and Electrochemical Measurements

All the electrochemical experiments were conducted using vacuum-sealed pouch-type electrochemical cells. The conventional 2-electrode LFP-Li cells were assembled in an Ar-filled glove box using pre-prepared circular cathodes as the working electrodes and a circular metallic lithium foil (geometric area of 2.5 cm^2) as the counter electrode. The lithium foil used to prepare the lithium anodes was immediately scratched and manually rolled in a glove box to remove the surface layer(s), thus yielding a freshly exposed shiny surface. We used glass-fiber filter paper (Whatman, GF/A glass microfiber) with a geometric area of 3.5 cm^2 and thickness of $260 \mu\text{m}$ (non-compressed) and approximately $200 \mu\text{m}$ (when squeezed in an assembled cell). The electrolyte used was a commercial “LP-40” 1 M solution of LiPF_6

Table 1. Specifications of the testing cells used in the present study.

Cell no.	Active material (AM)	Electrode composition AM:CB:PVdF [wt%]	Electrode parameters		Measurement, DOD at stopping
			AM mass loading [mg cm ⁻²]	Porosity [vol%]	
#1	Targray LFP	90: 5: 5	4.5	41 ± 1	Baseline, current stimuli, complete C/100 cycle
#2	Targray LFP with selected particle size/aggregation	90: 5: 5	0.6	≈50	Baseline, DOD = 0.5
#3	Targray LFP with selected particle size/aggregation	90: 5: 5	0.6	≈50	Current stimuli, DOD = 0.51
#4	LFP by PCR-method	90: 5: 5	4.1	43 ± 1	Parallel battery experiment
#5	LFP by PCR-method	90: 5: 5	4.1	43 ± 1	Parallel battery experiment
#6	LFP by PCR-method	90: 5: 5	2.1	43 ± 1	EIS measurements, DOD = 0.9
#8	LFP by PCR-method	90: 5: 5	3.1	43 ± 1	Current stimuli of base –C/5
#9	LFP by PCR-method	90: 5: 5	3.4	43 ± 1	Current stimuli in both directions (effect of electrode thickness)
#10	LFP by PCR-method	90: 5: 5	0.3	≈43	Current stimuli in both directions (effect of electrode thickness)
#11	Targray LFP	5: 73: 22	0.018*	75 ± 2	Baseline, current stimuli (variation of stimuli duration)
#12	Targray LFP	90: 5: 5	4.5	41 ± 1	Baseline, current stimuli, complete C/100 cycle
#13	Targray LFP	90: 5: 5	3.1	41 ± 1	Baseline, current stimuli
#14	LMP	80: 10: 10	0.4	≈54	Baseline, current stimuli (variation of baseline current magnitude)
#15	LFP by PCR-method	90: 5: 5	3.3	43 ± 1	Current stimuli (variation of baseline current magnitude)

Provided is the information about the type of active insertion material (AM), (dry) electrode composite composition (CB = carbon black, PVdF = polyvinylidene difluoride binder), electrode parameters, and the type of electrochemical measurement. "LFP by PCR method" denotes LFP material synthesized in-house by the PCR method. *Cathode with "diluted LFP" contains an extremely low mass fraction of LFP and very high mass fraction of CB—effectively providing good electronic and ionic wiring of the AM. All the cells presented in Table 1 included an LFP-based cathode and lithium-metal anode.

in ethylene carbonate/diethyl carbonate (EC:DEC = 1:1 wt/wt, Merck).

Before all the current stimulus experiments, the LFP-Li cells with "pristine" LFP electrodes were galvanostatically pre-cycled with C/10 (5 cycles) in the voltage window 2.7–4.1 V, followed by a +C/10 charge up to 3.9 V vs Li, potential hold for 6 h at 3.9 V, and relaxation at OCV for 6 h. This implies that the cells were free of initial cycling effects, and the global DOD of the LFP electrodes was driven outside the 2-phase regime to be close to 0 ($x \approx 0$ in Li_xFePO_4). A similar pre-cycling routine was applied for LMP-Li cells (3 cycles at C/20 in voltage window 2.7–4.5 V). All the galvanostatic and impedance electrochemical experiments were performed using a "VPM3" (Bio-Logic) potentiostat/galvanostat running with EC-Lab software. For the dedicated experiment with the LFP-Li cell, in which we measured the impedance response after partial discharge into the plateau region of the LFP, we used a small-amplitude (5 mV) sinusoidal perturbation in the frequency range of 20 kHz to 0.2 mHz. We have

deliberately used a low number of measured points (3 points per decade of frequency sweep) to reduce the measurement time to a minimum and thus minimize the effect of further cell relaxation. To diminish the effects of surrounding temperature variation, all the measurements were performed by keeping the battery cell temperature constant in a thermostatic bath (dipped in silicone oil with a temperature of 25 ± 0.1 °C). The specifications of all the electrochemical cells used in the current study are listed in Table 1.

4.4. Sample Preparation for Scanning Transmission Electron Microscopy – Electron Energy-Loss Spectroscopy (STEM-EELS) Experiments

The particles of the Li_xFePO_4 electrode material were obtained from the LFP cathodes that were subjected to selected electrochemical protocols in the corresponding LFP-Li cells as follows. We conducted two main electrochemical experiments (baseline

and current stimuli) and two additional experiments for the Fe²⁺ and Fe³⁺ references. Initially, the LFP-Li cells were pre-cycled (3 cycles at C/10 in voltage range 2.5–4.1 V), followed by slow +C/20 charge and 20-h voltage hold at 3.8 V to achieve complete delithiation and thus drive all the active particles in equilibrium Li-poor solid solution (FP) corresponding to the thermodynamic state at 3.8 V vs Li. The cell used to obtain material for the Fe³⁺ reference was stopped under these conditions. For the baseline experiment, the cell was discharged by –C/100 down to DOD = 0.5. For the experiment with electrode activation, the cell was first discharged by –C/100 down to DOD = 0.25, followed by –5C current stimuli until DOD = 0.5, and finally discharged for 50 min with –C/100 exactly to the point corresponding to the local maximum of the voltage curve (Figure 1a). The cell that was used to obtain the material for the Fe²⁺ reference was discharged by slow C/20 discharge, followed by a 20 h voltage hold at 2.7 V to complete lithiation and thus drive all the active particles in the equilibrium Li-rich solid solution (LFP) corresponding to the thermodynamic state at 2.7 V vs Li.

All samples of the LFP/FP (Li_xFePO₄) particles were obtained from the corresponding cells by transferring them rapidly into an Ar-filled glove box, followed by fast disassembly and washing of the cathode in 40 mL of high-purity anhydrous diethyl carbonate (DEC, Sigma-Aldrich) for 5 min (with stirring). The washed electrode was allowed to dry in a glove box for approximately 2 min. This indicates that the electrolyte was removed from the cathode and further relaxation of the local Li_xFePO₄ composition within the particles was significantly diminished (inhibited).^[11] The inspected electrode was dipped in 3 mL of Ar-purged Ethyl acetate, sealed, and transferred to an ultrasound (US) bath. After 20 min of electrode exposure to US agitation, the dispersion was allowed to settle down (10 min), followed by pipetting out 10 μL of the dispersion of particles and drop casting them onto a Cu lacey TEM grid. After drying for 2 min, the grid was placed in an Ar-filled container and sealed for transfer to the TEM room (within 3 min). The grid was mounted onto a TEM holder and inserted into the microscope within 1 min. The total exposure of the sample(s) to air was less than 3 min.

4.5. STEM-EELS Measurements

STEM-EELS observations were performed using a cold-field emission gun and a Cs-corrected JEOL ARM microscope equipped with a GIF Quantum (Gatan) Dual EELS spectrometer. The acceleration voltage was set to 200 kV and the estimated electron-beam current was ≈48.9 pA. The convergence and EELS collection semi-angles were 18 and 60 mrad, respectively. Maps and standards spectra were collected using an energy dispersion of 0.1 and 0.25 eV per channel in the spectrometer. The exposure time during mapping acquisition was 0.5 s per pixel using a sub-pixel scan. Different pixel sizes ranging from 5 to 14 nm were used depending on the size of the particles. The chemical maps for the determination of the local Fe²⁺/Fe³⁺ composition (LFP/FP phases) in the individual LFP particles were analyzed using multiple linear least squares (MLLS) fitting. More technical details concerning EELS data collection and a description of the analysis

of the measured EELS mappings are presented in Section S2 of the Supporting Information.

5. Brief Description of the Simulation Model

The primary aim of the simulation results was to provide a bridge between the thermodynamic reasoning presented in Figure 3 and the experimental evidence presented in Figure 1. The specific goal was to explain the first-order experimental phenomena observed in this study, that is, the pulse effect. For clarity and generality, various details might further improve the fitting of secondary characteristics of measured curves, but are not essential for the explanation of the pulse effect, as this would be beyond the scope of the current study. The simulation model is described in more detail in Section S6.1, Supporting Information. In the following paragraphs, we outline its general characteristics.

Simulations were conducted using an extended continuum-level porous electrode model inspired by the porous electrode theory,^[61,62] which was upgraded to more consistently represent the electrode topology and material characteristics. It is based on the governing equations for the concentration of ionic species in the electrolyte and liquid, as well as the solid-phase potential. These equations are solved under the assumption of electroneutrality, while considering the widely adopted Butler-Volmer equation, with the exchange current density derived from the regular solution theory^[63] to model the charge-transfer molar flux coupling the transport between the electrolyte and the solid domain.

Another merit of the applied modeling framework is the plausible determination of the chemical potential of active particles via a multiscale approach that preserves a high level of consistency with lower scales and thus increases the modeling fidelity of the cathode (elaborated in references^[48,64,65]). Owing to their relatively small size and short characteristic diffusion times,^[15] the particles were simulated as 0D particles^[65] with a chemical potential derived through a consistent reduction of the detailed spatially resolved model relying on the regular solution theory for phase-separating materials.^[64] This 0D virtual representation of particles is necessary to ensure finite computational times when performing electrode-level simulations that are required to virtually represent the electric performance response of the battery, which comprises a large number of particles.

The model considers that the equilibrium chemical potential is inherently linked to the lithiation level of a particle and thus to mass conservation in the active particle, which is very important for modeling the redistribution of Li between active particles via the electrolyte or direct contact by considering the real electrode topology and material properties.^[48] For the simulations of the half-cell, a 2D unstructured mesh with 273 control volumes was used.

The applied approach thus opens possibilities for long-term dynamic simulations of the entire electrochemical cell or half-cell while considering the specific topological characteristics of the materials, which are crucial for the credible analyses of the path-dependent entrance into the voltage hysteresis in phase-separating battery materials.

Supporting Information

Supporting Information is available from the Wiley Online Library or from the author.

Acknowledgements

The authors acknowledge financial support from the Slovenian Research Agency (research core funding No. P2-0401 and P2-0393 and projects J7-8270 and J2-2494). This project had received funding from the European Union's Horizon 2020 Research and Innovation Programme under grant agreement No. 769506. The authors acknowledge the help of Andrej Debenjak for providing a dedicated in-house build amplifier and technical support during the implementation of the parallel battery experiment. The authors greatly acknowledge the help of Marjan Bele for performing SEM analysis and sharing many suggestions during the preparation of material for STEM-EELS experiments.

Conflict of Interest

The authors declare no conflict of interest.

Author Contributions

T.K. and J.M. contributed equally to this work and should be considered joint first authors. The concept for this work was defined by T.K., K.Z., and M.G.; T.K. and K.Z. elaborated and performed the thermodynamic analysis; J.M. synthesized materials and electrodes and performed measurements; F.R.-Z. and J.M. conducted STEM-EELS experiments and analysis. T.K., K.Z., and I.M. conceived the simulation model, I.M. performed simulations; T.K., K.Z., and M.G. wrote the draft manuscript with input from all authors; all authors reviewed & edited the final manuscript.

Data Availability Statement

The data that support the findings of this study are openly available in Zenodo at <https://zenodo.org/record/7351529#.Y34o533MJPY>.

Keywords

batteries, intraparticle phase-separation, lithium iron phosphate, phase-separating materials, voltage hysteresis

Received: November 23, 2022
Revised: April 24, 2023
Published online: June 25, 2023

- [1] R. Malik, *Joule* **2018**, 2, 2204.
- [2] R. Malik, *Joule* **2018**, 2, 1923.
- [3] Z. Wang, G. Feng, D. Zhen, F. Gu, A. Ball, *Energy Rep.* **2021**, 7, 5141.
- [4] M. A. Hannan, M. H. Lipu, A. Hussain, A. Mohamed, *Renewable Sustainable Energy Rev.* **2017**, 78, 834.
- [5] J. K. Barillas, J. Li, C. Günther, M. A. Danzer, *Appl. Energy* **2015**, 155, 455.
- [6] J. Li, Q. Lai, L. Wang, C. Lyu, H. Wang, *Energy* **2016**, 114, 1266.
- [7] D. Li, Y. Sun, Z. Yang, L. Gu, Y. Chen, H. Zhou, *Joule* **2018**, 2, 1265.
- [8] X. Jin, Y. Han, Z. Zhang, Y. Chen, J. Li, T. Yang, X. Wang, W. Li, X. Han, Z. Wang, X. Liu, H. Jiao, X. Ke, M. Sui, R. Cao, G. Zhang, Y. Tang, P. Yan, S. Jiao, *Adv. Mater.* **2022**, 2109356.

- [9] C. Delmas, M. Maccario, L. Croguennec, F. Le Cras, F. Weill, *Nat. Mater.* **2008**, 7, 665.
- [10] W. Dreyer, J. Jamnik, C. Gohlke, R. Huth, J. Moškon, M. Gaberšček, *Nat. Mater.* **2010**, 9, 448.
- [11] Y. Li, H. Chen, K. Lim, H. D. Deng, J. Lim, D. Fraggadakis, P. M. Attia, S. C. Lee, N. Jin, J. Moškon, Z. Guan, W. E. Gent, J. Hong, Y.-S. Yu, M. Gaberšček, M. Saiful Islam, M. Z. Bazant, W. C. Chueh, *Nat. Mater.* **2018**, 17, 915.
- [12] R. Malik, *Joule* **2018**, 2, 1213.
- [13] R. Malik, F. Zhou, G. Ceder, *Nat. Mater.* **2011**, 10, 587.
- [14] M. Z. Bazant, *Acc. Chem. Res.* **2013**, 46, 1144.
- [15] P. Bai, D. A. Cogswell, M. Z. Bazant, *Nano Lett.* **2011**, 11, 4890.
- [16] T. Sasaki, Y. Ukyo, P. Novak, *Nat. Mater.* **2013**, 12, 569.
- [17] A. Van der Ven, K. A. See, L. Pilon, *Battery Energy* **2022**, 1, 20210017.
- [18] A. V. Neimark, P. I. Ravikovitch, A. Vishnyakov, *Phys. Rev. E* **2002**, 65, 031505.
- [19] I. Müller, H. Xu, *Acta Metall. Mater.* **1991**, 39, 263.
- [20] S. Fu, I. Müller, H. Xu, *MRS Online Proc. Lib.* **1991**, 246, 39.
- [21] M. Gurrvitch, S. Luryi, A. Polyakov, A. Shabalov, *J. Appl. Phys.* **2009**, 106, 104504.
- [22] J. R. Pomeroy, E. D. Sontag, J. E. Ferrell, *Nat. Cell Biol.* **2003**, 5, 346.
- [23] R. Sessoli, D. Gatteschi, A. Caneschi, M. Novak, *Nature* **1993**, 365, 141.
- [24] E. Coronado, J. R. Galán-Mascarós, M. Monrabal-Capilla, J. Garcia-Martinez, P. Pardo-Ibáñez, *Adv. Mater.* **2007**, 19, 1359.
- [25] E. M. Ozbudak, M. Thattai, H. N. Lim, B. I. Shraiman, A. Van Oudenaarden, *Nature* **2004**, 427, 737.
- [26] Y. Zhu, Y. Xu, Y. Liu, C. Luo, C. Wang, *Nanoscale* **2013**, 5, 780.
- [27] J. Wang, X. Sun, *Energy Environ. Sci.* **2015**, 8, 1110.
- [28] M. Wagemaker, F. M. Mulder, *Acc. Chem. Res.* **2013**, 46, 1206.
- [29] J. Lim, Y. Li, D. H. Alsem, H. So, S. C. Lee, P. Bai, D. A. Cogswell, X. Liu, N. Jin, Y.-s. Yu, N. J. Salmon, D. A. Shapiro, M. Z. Bazant, T. Tyliczszak, W. C. Chueh, *Science* **2016**, 353, 566.
- [30] M. Brokate, J. Sprekels, *Hysteresis and Phase Transitions, Applied Mathematical Sciences*, vol. 121, Springer, New York, **1996**.
- [31] Y. Jiang, G. Offer, J. Jiang, M. Marinescu, H. Wang, *J. Electrochem. Soc.* **2020**, 167, 130533.
- [32] D. R. Baker, M. W. Verbrugge, X. Xiao, *J. Appl. Phys.* **2017**, 122, 165102.
- [33] Q. Zhang, Y. Cui, E. Wang, *Modell. Simul. Mater. Sci. Eng.* **2013**, 21, 074001.
- [34] X. Zhang, M. Van Hulzen, D. P. Singh, A. Brownrigg, J. P. Wright, N. H. Van Dijk, M. Wagemaker, *Nat. Commun.* **2015**, 6, 8333.
- [35] W. C. Chueh, F. El Gabaly, J. D. Sugar, N. C. Bartelt, A. H. McDaniel, K. R. Fenton, K. R. Zavadil, T. Tyliczszak, W. Lai, K. F. McCarty, *Nano Lett.* **2013**, 13, 866.
- [36] H. Liu, S. Kazemiabnavi, A. Grenier, G. Vaughan, M. Di Michiel, B. J. Polzin, K. Thornton, K. W. Chapman, P. J. Chupas, *ACS Appl. Mater. Interfaces* **2019**, 11, 18386.
- [37] J. L. Jones, J.-T. Hung, Y. S. Meng, *J. Power Sources* **2009**, 189, 702.
- [38] D. Robert, T. Douillard, A. Boulineau, G. Brunetti, P. Nowakowski, D. Venet, P. Bayle-Guillemaud, C. Cayron, *ACS Nano* **2013**, 7, 10887.
- [39] Y. Li, F. El Gabaly, T. R. Ferguson, R. B. Smith, N. C. Bartelt, J. D. Sugar, K. R. Fenton, D. A. Cogswell, A. L. D. Kilcoyne, T. Tyliczszak, M. Z. Bazant, W. C. Chueh, *Nat. Mater.* **2014**, 13, 1149.
- [40] J. Lim, Y. Li, D. H. Alsem, H. So, S. C. Lee, P. Bai, D. A. Cogswell, X. Liu, N. Jin, Y.-S. Yu, N. J. Salmon, D. A. Shapiro, M. Z. Bazant, T. Tyliczszak, W. C. Chueh, *Science* **2016**, 27, 566.
- [41] H. Liu, F. Strobridge, *Science* **2014**, 344, 6191.
- [42] X. Zhang, M. Van Hulzen, D. P. Singh, A. Brownrigg, J. P. Wright, N. H. Van Dijk, M. Wagemaker, *Nano Lett.* **2014**, 14, 2279.

- [43] D. Walter, in *Nanomaterials*, Ed.: Deutsche Forschungsgemeinschaft, Wiley-VCH, Weinheim, Germany **2013**, p. 9.
- [44] T. Zhang, M. Kamlah, *J. Electrochem. Soc.* **2020**, *167*, 020508.
- [45] J. D. Sugar, F. El Gabaly, W. C. Chueh, K. R. Fenton, T. Tyliszczak, P. G. Kotula, N. C. Bartelt, *J. Power Sources* **2014**, *246*, 512.
- [46] Y. Li, S. Meyer, J. Lim, S. C. Lee, W. E. Gent, S. Marchesini, H. Krishnan, T. Tyliszczak, D. Shapiro, A. L. D. Kilcoyne, W. C. Chueh, *Adv. Mater.* **2015**, *27*, 6591.
- [47] Y.-S. Yu, C. Kim, D. A. Shapiro, M. Farmand, D. Qian, T. Tyliszczak, A. D. Kilcoyne, R. Celestre, S. Marchesini, J. Joseph, P. Denes, T. Warwick, F. C. Strobridge, C. P. Grey, H. Padmore, Y. S. Meng, R. Kostecki, J. Cabana, *Nano Lett.* **2015**, *15*, 4282.
- [48] I. Mele, I. Pačnik, K. Zelič, J. Moškon, T. Katrašnik, *J. Electrochem. Soc.* **2020**, *167*, 060531.
- [49] J. Dambrowski, in *INTELEC 2013 The 35th Int Telecommunication Energy Conf*, **2013**, <https://www.deutronic.de/wp-content/uploads/2021/02/Review-on-Methods.pdf>.
- [50] M. P. Mercer, C. Peng, C. Soares, H. E. Hoster, D. Kramer, *J. Mater. Chem. A* **2021**, *9*, 492.
- [51] MAX17852 –14-Channel High-Voltage, ASIL D, Data-Acquisition System with Integrated Current-Sense Amplifier, <https://www.analog.com/media/en/technical-documentation/datasheets/max17852.pdf>, (accessed: November 2022).
- [52] MAX14921 – High-Accuracy 12-/16-Cell Measurement AFEs, <https://www.analog.com/en/products/max14921.html#product-overview>, (accessed: November 2022).
- [53] Orion BMS2 – Lithium Ion Battery Management System Specifications, https://www.orionbms.com/downloads/documents/orionbms2_specifications.pdf, (accessed: November 2022).
- [54] D. Burch, M. Z. Bazant, *Nano Lett.* **2009**, *9*, 3795.
- [55] D. A. Cogswell, M. Z. Bazant, *Nano Lett.* **2013**, *13*, 3036.
- [56] B. Orvananos, R. Malik, H. C. Yu, A. Abdellahi, C. P. Grey, G. Ceder, K. Thornton, *Electrochim. Acta* **2014**, *137*, 245.
- [57] G. Križan, J. Križan, R. Dominko, M. Gaberšček, *J. Power Sources* **2017**, *363*, 218.
- [58] G. Križan, J. Križan, I. Bajsić, M. Gaberšček, *Instrum. Sci. Technol.* **2018**, *46*, 43.
- [59] C. Fongy, S. Jouanneau, D. Guyomard, J. C. Badot, B. Lestriez, *J. Electrochem. Soc.* **2010**, *157*, A1347.
- [60] C. Fongy, A.-C. Gaillot, S. Jouanneau, D. Guyomard, B. Lestriez, *J. Electrochem. Soc.* **2010**, *157*, A885.
- [61] J. Newman, W. Tiedemann, *AIChE J.* **1975**, *21*, 25.
- [62] M. Doyle, T. F. Fuller, J. Newman, *J. Electrochem. Soc.* **1993**, *140*, 1526.
- [63] B. Orvananos, T. R. Ferguson, H.-C. Yu, M. Z. Bazant, K. Thornton, *J. Electrochem. Soc.* **2014**, *161*, A535.
- [64] K. Zelič, T. Katrašnik, *Sci. Rep.* **2019**, *9*, 2123.
- [65] K. Zelič, T. Katrašnik, *J. Electrochem. Soc.* **2019**, *166*, A3242.